Journal of Power Sources 635 (2025) 236535

Contents lists available at ScienceDirect

Journal of Power Sources

journal homepage: www.elsevier.com/locate/jpowsour

Conjugated microporous polymers incorporating pyridine moieties for efficient faradaic supercapacitor energy storage

Shimaa Abdelnaser [a,b], Shiao-Wei Kuo [a], Ahmed F.M. EL-Mahdy [a,b,*]

[a] Department of Materials and Optoelectronic Science, National Sun Yat-Sen University, Kaohsiung, 80424, Taiwan
[b] Chemistry Department, Faculty of Science, Assiut University, Assiut, 71516, Egypt

HIGHLIGHTS

- Triphenylpyridine-based CMPs were developed for Faradaic supercapacitors.
- CMPs demonstrated a capacitance of 221.86 F g^{-1} at a current density of 0.5 A g^{-1}.
- CMP-based symmetric supercapacitor device exhibited a capacitance of 384.61 F g^{-1}.
- The device exhibited an energy density of 77.13 W h kg^{-1} and 461.53 W kg^{-1}.

GRAPHICAL ABSTRACT

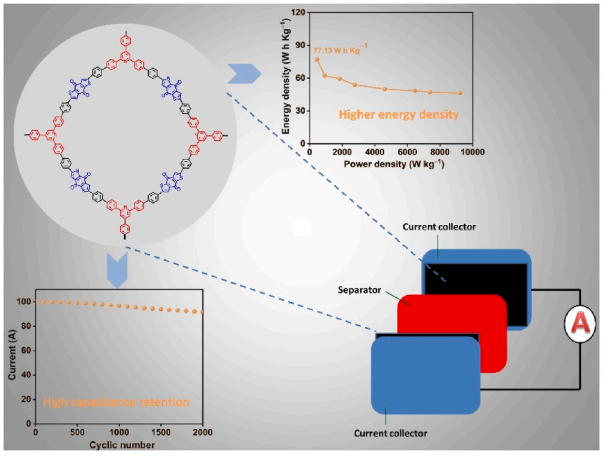

ARTICLE INFO

Keywords:
Conjugated microporous polymers
Redox-active polymers
Triphenylpyridine
Planarity
Benzo[1,2-b:4,5-b']dithiophene-4,8-dione
Supercapacitors

ABSTRACT

Conjugated microporous polymers (CMPs) are significant materials owing to their π-conjugated frameworks and microporous architecture. However, several CMPs have limited electrical conductivity and redox efficiency, making them unsuitable as dynamic supercapacitor electrodes. In this work, we prepared a particular family of redox-active CMPs, namely TPP-DBTh and BTPP-DBTh CMPs, with triphenylpyridine (TPP) and redox-active benzo[1,2-b:4,5-b′]dithiophene-4-dione (DBTh) units for effective supercapacitor energy storage devices. Combining TPP and redox-active DBTh units into CMP skeletons promotes faradaic energy storage, charge transfer, and conductivity. The final CMPs demonstrate a superior specific capacity relative to previously published conventional CMPs, achieving an impressive three-electrode capacitance of up to 221.86 F g^{-1} at a current density of 0.5 A g^{-1}, along with remarkable stability of up to 87.86 % within 10,000 cycles, marking this as one of the highest specific capacities recorded for CMPs. The TPP-DBTh CMP produces a symmetric two-electrode supercapacitor device, which can maintain 91.81 % of their initial capacitance after 2000 cycles. The TPP-DBTh CMP-based device has a high capacitance of 384.61 F g^{-1}, energy density of 77.13 W h kg^{-1}, and

* Corresponding author. Department of Materials and Optoelectronic Science, National Sun Yat-Sen University, Kaohsiung, 80424, Taiwan.
E-mail address: ahmedelmahdy@mail.nsysu.edu.tw (A.F.M. EL-Mahdy).

https://doi.org/10.1016/j.jpowsour.2025.236535
Received 22 October 2024; Received in revised form 11 February 2025; Accepted 12 February 2025
Available online 19 February 2025

power density of 461.53 W kg^{-1} at 1.2 V. Our findings offer a straightforward method for combining electroactive moieties to create effective supercapacitor devices.

1. Introduction

The main source of energy for many years has been fossil fuels. However, they have a lot of problems, such as releasing a lot of carbon dioxide (CO_2) into the air, changing the climate, using up resources quickly, and having negative effects on health [1]. Hence, scientists are actively exploring various methods to face the challenges associated with energy storage [2]. One of the most important ways to deal with energy shortages is to store energy electrochemically. Under the charging and discharging process, this technology transforms electrical energy into chemical energy [3]. The most common types of electrochemical energy storage systems are batteries and supercapacitors (SCs). Because of many advantages of SCs, such as higher energy and power density, rapid charge/discharge kinetics, enlarged cycle life, safety, and renewability, SCs have found more applications in industry, particularly in transportation like electric buses, trams, and trains for rapid energy storage and release during acceleration and deceleration [4,5]. Supercapacitors can store energy through chemical reactions or physical dissociation between electrolyte ions and carbon electrodes [6,7]. As a result, the electrode material is considered the main parameter controlling the efficacy of SCs [8–10]. The storage of energy in supercapacitors is primarily achieved through two main mechanisms: 1) in pseudocapacitors, through faradaic reactions between the electrolyte and electrode moieties (such as metal oxides), and 2) in electrical double-layer capacitors (EDLCs), through the adsorption and desorption of electrically charged ions at the electrode interface (such as porous carbon) [11]. Transition-metal oxides such as MnO_2 and Fe_2O_3 are often used in pseudocapacitors [12]. Nevertheless, rapid redox reactions sometimes lead to the expansion and contraction of the electrodes, resulting in a decrease in their mechanical durability and rendering their active sections unavailable [13]. Contrarily, carbonaceous materials such as activated carbon, graphene, and carbon nanofibers are used in EDLC [14]. Because carbon does not contain any electroactive sites, SCs made of carbon exhibit excellent rate performance, a high density, and a long lifetime. However, their characteristic capacitance and density of energy are low [15]. For the development of high-performance supercapacitors, it is imperative to employ electrode materials that exhibit superior intrinsic conductivity, incorporate designs that allow for variable porosity, maintain stable structural topologies, and include a redox-active functional group.

Porous organic polymers (POPs) are porous materials that are important in energy storage devices because of their unique properties such as strong covalent bonds, high surface area, large pore volume, high porosity, low mass density, good chemical and thermal stability [16–19]. Conjugated microporous polymers (CMPs) are a type of porous material that is gaining increasing attention. These materials show great promise for various applications in energy and environmental protection [20]. CMPs are three-dimensional macromolecules with pore sizes ranging from micro-to meso-porous scale, formed by covalent bonds [21]. Several unique properties distinguish CMPs from traditional polymers. These include delocalized conjugation, good surface area, uniform micropores, stability under hard conditions, durability, structural tunability, and the simplicity of functionalization with different types of organic groups [22,23]. Additionally, CMPs are used in many applications, such as gas separation, catalysis, sensing, optical applications, drug delivery, energy, and environmental fields [24–29]. Considering electrochemistry, CMPs have unique electrochemical properties above conventional polymers since they may include certain redox active constituents into their structures through modifying their building linkages. They ought to additionally possess fast ion diffusion rates and are resistant to the random folding issue since their specific porosity feature allows the highest feasible interaction with heteroatomic active sites [16,30,31]. So, it is expected that using CMPs to store electrochemical energy would lead to a substantial amount of storage.

In the fabrication of electrodes composed of conjugated microporous polymers (CMPs), it is a prevalent methodology to amalgamate them with supplementary conductive materials to enhance their electrical conductivity. However, the insufficient interfacial adhesion between the CMPs and the conductive additives poses a significant challenge in markedly improving the performance of CMP-based electrodes [32,33]. By including redox-active units into the skeletons of CMPs, such as ferrocene, anthraquinone, porphyrin derivatives, phenazine, and aza-fused rings, it is possible to increase the conductivity of CMPs when they are structurally formed [21,34–38]. This is an alternative method for increasing the capacitance of CMPs. Such specific components now limit the variety of redox-active functionalities that may be included in the frameworks of CMPs to serve as novel electrode materials. Although redox-based CMPs have prospective redox behavior and elevated capacitance. Because of this, developing new redox-active CMPs that have superior conductivity and electrochemical endurance throughout charge-discharge cycles is necessary to improve the performance of supercapacitors.

Heteroatom (N, B, O, S) functionalization can create layered interrelated pore structures that boost graphene's interlayer separating and moisture absorption, revealing an improved obtainable surface and rich electroactive regions. This activates the ring and increases its redox activity, which raises the electron cloud density of carbon atoms on the ring [39]. In addition, functionalized pyridine belongs to a significant group of heterocyclic compounds. Many substituted pyridines play a big part in catalysis and material science [40]. Furthermore, due to its possible charge-transporting and electron-donating properties, benzo[1,2-b:4,5-b′]dithiophene-4-dione analogs have been employed as building appealing polymers in solar cells [11]. No one has ever reported or examined the use of CMP skeletons, including triphenylpyridine (TPP) and redox-active benzo[1,2-b:4,5-b′]dithiophene-4-dione (DBTh) moieties for applications in supercapacitor technology. In this study, we synthesized two redox-active TPP- and DBTh-based CMPs (TPP-DBTh and BTPP-DBTh) by Suzuki–Miyaura reaction for supercapacitor application. The TPP-DBTh CMP was prepared through the interaction of 2,4,6-tris(4-bromophenyl)pyridine (TPP-3Br) (Scheme S2), 1,4-phenylenediboronic acid (Ph-2BO) and 2,6-dibromobenzo[1,2-b:4,5-b']dithiophene-4,8-dione (DBTh-2Br) (Scheme S1) in DMF, while 1,4-bis(2,6-bis(4-bromophenyl)pyridin-4-yl)benzene (BTPP-4Br) (Scheme S3) (Ph-2BO), and (DBTh-2Br) were used to prepare the BTPP-DBTh CMP (Schemes S4, S5, and 1). By incorporating TPP and redox-active DBTh into the skeleton of CMPs, our study showed that it is possible to build electrode materials based on CMPs that possess pseudocapacitive properties and an exceptional specific capacity. An exceptional specific capacity of 221.86 F g^{-1} was exhibited by the redox-active TPP- and DBTh-based CMPs. This results in a higher specific capacity than the standard CMPs that were reported in the past. Following 10,000 charge–discharge cycles, a retention of 77.45 % of the initial capacitance was observed, marking a notable achievement among analogous materials. Moreover, it is feasible to fabricate both symmetric two-electrode and three-electrode capacitor devices utilizing TPP- and DBTh-based CMPs, facilitating efficient charge energy storage.

2. Experimental

2.1. Characterizations

FTIR spectroscopy has been investigated employing a Bruker Tensor 27 FTIR spectrophotometer. Bruker Avance 400 NMR spectroscopy was used for the collection of SSNMR spectra. TGA was accomplished with a TA Q-50 analyzer. Additional characterizations of the synthesized CMPs are provided in the Supporting Information (Section S2. Characterization).

2.2. General preparation of TPP-DBTh CMP

A mixture of TPP-3Br (0.276 mmol), Ph-2BO (0.827 mmol), DBTh-2Br (0.414 mmol) and tetrakis(triphenylphosphine)palladium(0) (0.0275 mmol) were put in a Pyrex tube (50 mL). Then DMF (25 mL) and potassium carbonate (550 mg in 5 mL of water) were added. Purging the reaction mixture with N_2 after three freeze–pump–thaw cycles removed oxygen. The tube was kept at 130 °C for three consecutive days. Following cooling to 25 °C, the reaction slurry was centrifuged and washed with acetone (three times) and THF (three times) until colorless. The resulting solid was air-dried at 100 °C overnight under a vacuum to obtain TPP-DBTh CMP as a reddish-brown solid.

2.3. General preparation of BTPP-DBTh CMP

A mixture of BTPP-4Br (0.176 mmol), Ph-2BO (0.706 mmol), 2 DBTh-2Br (0.352 mmol) and tetrakis(triphenylphosphine)palladium(0) (0.018 mmol) were put in a Pyrex tube (50 mL). Then DMF (25 mL) and potassium carbonate (550 mg in 5 mL of water) were added. Purging the reaction mixture with N_2 after three freeze–pump–thaw cycles removed oxygen. The tube was kept at 130 °C for three consecutive days. Following cooling to 25 °C, the reaction slurry was centrifuged and washed with acetone (three times) and THF (three times) until colorless. The resulting solid was air-dried at 100 °C overnight under a vacuum to obtain BTPP-DBTh CMP as an orange solid.

2.4. Electrochemical Analysis

For the Three-Electrode System, electrochemical studies were conducted in a three-electrode cell utilizing an Autolab potentiostat (PGSTAT204) with a 3 M KOH aquatic medium. The GCE served as the working electrode. Platinum wire served as the counter electrode, while Hg/HgO (RE-61AP, BAS) functioned as the reference electrode. Cyclic voltammetry (CV) with sweep rates ranging from 5 to 200 mV s^{-1} and galvanostatic charge-discharge (GCD) with potentials ranging from 0.0 to −0.7 V vs. Hg/HgO and current densities ranging from 0.5 to 20 A g^{-1} were used to study the electrochemical performance. Supporting Information (section S10. Electrochemical Analysis in Three-Electrode System) contains more details on the electrochemical investigation of the three-electrode system.

For the two-electrode symmetric supercapacitor system, the slurry was made by combining CMP (70 wt %), carbon black (20 wt %), and Nafion (10 wt %). It was applied onto 0.1 mm Kuraray carbon paper having a 1 cm × 1 cm target area and dried overnight at 100 °C in a vacuum oven. On a single current collector, active material mass loading was 1.35 mg cm^{-2}. Two working electrodes separated each other with filter paper and flooded with 3 M potassium hydroxide aqueous solution. Supporting Information (section S11. Electrochemical Analysis in Two-Electrode Symmetric Supercapacitor System) contains more details on the electrochemical investigation of the two-electrode system.

3. Results and discussion

3.1. The production and characterization of materials

The synthesis of the DBTh-2Br and TPP-3Br monomers followed established procedures (Schemes S1, S2, and Figs. S1–6) [11,41]. On the other hand, the synthesis of BTPP-4Br involved the reaction of 4-bromoacetophenone, terephthaldehyde, and ammonium acetate in acetic acid using a microwave apparatus (Scheme S3 and Figs. S7–9) [42]. The chemical composition of BTPP-4Br is validated using Fourier transform infrared (FTIR) and nuclear magnetic resonance (NMR) spectroscopy. The FTIR spectrum of BTPP-4Br exhibited distinct signals at 3069, 1599, 1546, 1176, and 625 cm^{-1}, corresponding to the vibrations of aromatic C–H, C = N, C=C, C–N, and C–Br bonds, respectively (Fig. S7). The ^1H NMR spectrum of BTPP-4Br displayed a doublet signal at 7.93 ppm, indicating the presence of aromatic C<u>H</u>−CBr groups. Additionally, other signals were observed at 8.10 and 7.66 ppm for the aromatic CH groups (Fig. S8). The ^{13}C NMR spectra of BTPP-4Br displayed a range of signals between 156.59 and 117.18 ppm, indicating the presence of aromatic carbon nuclei (Fig. S9). The new redox-active TPP-DBTh and BTPP-DBTh CMPs were synthesized using Suzuki-Miyaura coupling polymerization. This involved combining Ph-2BO and DBTh-2Br with TPP-3Br to produce TPP-DBTh CMP, which appeared as a non-soluble reddish-brown powder (Scheme 1 and S4). Similarly, coupling Ph-2BO and DBTh-2Br with BTPP-4Br resulted in BTPP-DBTh CMP forming, which also appeared as a non-soluble orange powder (Scheme 1 and S5). The insolubility of these CMPs in routinely employed organic solvents such as chloroform, alcohol, dioxane, or dimethylformamide indicates the presence of more robust crosslinked networks. The observed increase in crosslinking is likely due to a greater extent of coupling polymerization occurring during the synthesis process. The inductively coupled plasma-atomic emission spectroscopy (ICP-AES) analysis revealed that the purified TPP-DBTh and BTPP-DBTh products had palladium impurities in the amount of 0.015–0.029 mol%.

A variety of techniques, including FTIR, solid-state ^{13}C cross-polarization (CP)/magic angle spinning (MAS) NMR, thermogravimetric analysis (TGA), and X-ray photoelectron spectroscopy (XPS), were used to assess the chemical composition and thermal properties of TPP-DBTh and BTPP-DBTh materials (Fig. 1a and b). In the FTIR spectra of both CMPs, neither the C-Br bond oscillation signal at 637 cm^{-1} nor the B-O stretching bond oscillation signal at 1350 cm^{-1} were detected, collectively indicates successful Suzuki coupling polymerization (Figs. S10 and S11). The TPP-DBTh and BTPP-DBTh CMPs showed absorbing signals at 3031 and 3028 cm^{-1} for C–H aromatic bonding, 1644 and 1647 cm^{-1} for C=O, 1594 and 1601 cm^{-1} for C=N, and 1538 and 1536 cm^{-1} for C=C vibrations. The solid state ^{13}C NMR spectra of the two CMPs exhibited four main resonance regions at 132.67–120.92, 146.29–136.09, 155.58–147.51, and 182.56–171.76 ppm originating from the aromatic C–H, C–C, C–S, and C=O groups, respectively, for the TPP-DBTh and BTPP-DBTh CMPs (Fig. 1c). XPS is used to analyze the element types, and their chemical states present in CMPs. In Fig. S12, the S 2p, S 2s, O 1s, N 1s, C 1s, and orbitals have five highlighted peaks at 163.88, 228.31, 531.02, 397.14, and 284.23 eV for the TPP-DBTh CMP and 164.12, 228.09, 530.92, 397.13, and 284.34 eV for the BTPP-DBTh CMP. Therefore, the clean XPS spectra with no additional peaks indicate that the synthesized CMPs are relatively pure and free from significant contamination. Fig. 1d–g shows C 1s and S 2p orbital fittings in XPS spectra. These spectra show the peaks of our CMPs' carbon and sulfur species. The C 1s orbital of the TPP-DBTh CMP has five peaks: 283.59 eV for C=C bonds, 283.95 for C–C bonds, 284.37 for C–S bonds, 284.71 for C=N bonds, and 285.54 for C=O bonds (Fig. 1d and Table S1). The C 1s orbital of the BTPP-DBTh CMP has five peaks, as shown in Fig. 1e and Table S1, corresponding to 283.76 eV for the C=C bond, 284.33 for the C–C bond, 284.43 for the C–S bond, 284.81 for the C=N bond, and 285.38 for the C=O bond. The TPP-DBTh CMP has a C=C bond content of 72.35 %, C–C bond content of 6.55 %, C–S bond content of 12.59 %,

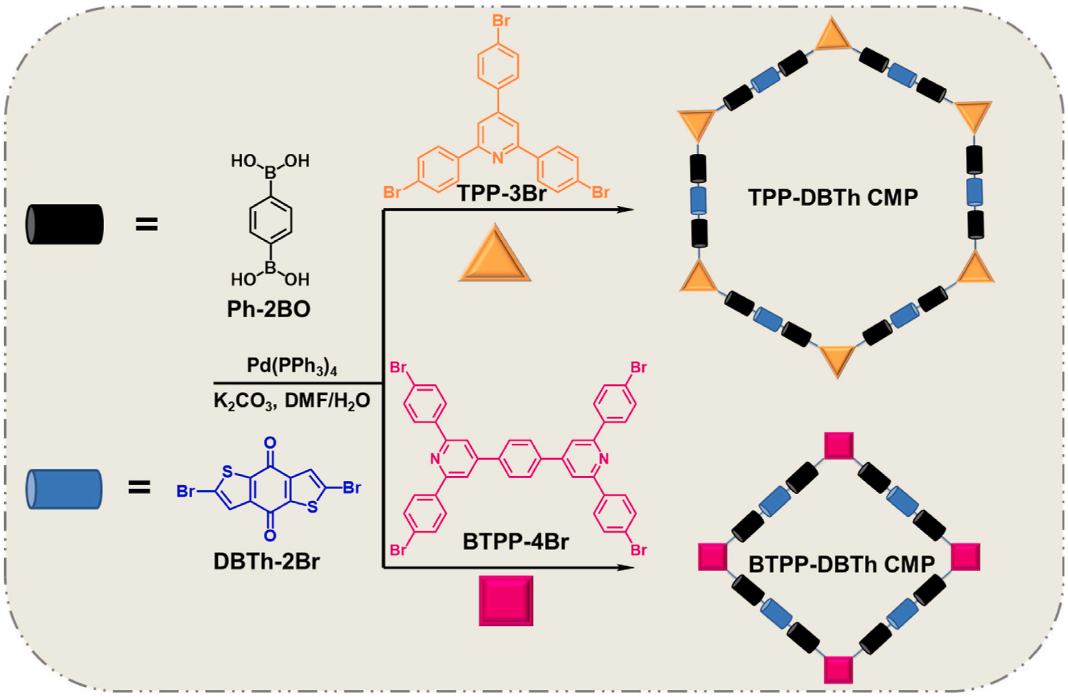

Scheme 1. Chemical synthesis and drawing scheme of TPP-DBTh and BTPP-DBTh CMPs.

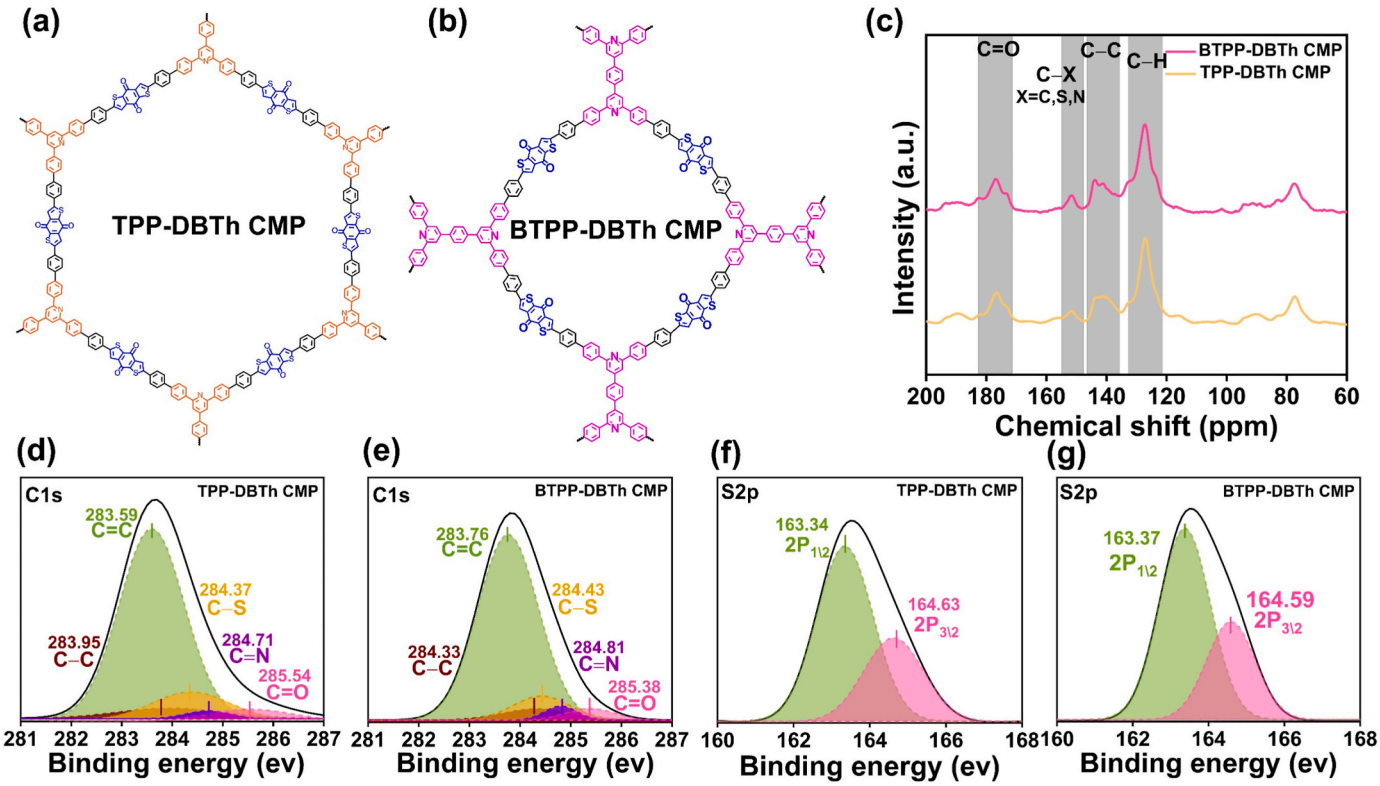

Fig. 1. (a,b) Chemical structures and (c) Solid-state ^{13}C NMR spectra of the TPP-DBTh and BTPP-DBTh CMPs. (d–g) XPS spectra of the (d) C1s and (f) S2p for the TPP-DBTh CMP and of (e) C1s and (g) S2p for the BTPP-DBTh CMP.

C=N bond content of 2.02 %, and C=O bond content of 6.49 %, while the BTPP-DBTh CMP has 78.2, 5.20, 9.51, 3.12, and 3.96 %, respectively (Table S2). TPP-DBTh CMP's S 2p orbital exhibited a pair around 163.34 and 164.63 eV, corresponding to both spinning orbits S $2p_{1/2}$ and S $2p_{3/2}$ that had a 2:1 proportion (Fig. 1f and Table S1), whereas BTPP-DBTh CMP's two spin orbits occurred at 163.37 and 164.59 eV. (Fig. 1g and Table S1). The experimental element ratio was determined by calculating the peak area of each species in the XPS survey of CMPs after the sensitivity factor adjustment. These two ratios are illustrated in Tables S3 and S4, which indicate a robust correlation. The present

investigation confirms that the TPP-DBTh CMP is formed via the interaction of Ph-2BO, DBTh-2Br, and TPP-3Br. Furthermore, we have confirmed that the interaction of Ph-2BO, DBTh-2Br, and BTPP-4Br forms the BTPP-DBTh CMP. Porous polymers must withstand severe conditions for electrochemical capacitors and other market energy storage devices. Hence, we explored the TPP-DBTh and BTPP-DBTh CMPs' thermal stability using TGA under a nitrogen-laden environment from 100 °C to 800 °C (Fig. S13 and Table S5). Fig. S13 and Table S5 show the results: the TPP-DBTh CMP achieved a T_{d10} equal 701.78 °C and a char yield that exceeded 83.61 %, while the BTPP-DBTh CMP had 596.81 °C and 76.51 %. The enhanced planarity of the TPP monomer within the CMP framework augmented the thermal stability of TPP-DBTh CMP compared to BTPP-DBTh CMP [43,44]. The elevated residual masses suggest that the polymers exhibit substantial cross-linking within their conjugated networks.

3.2. Porosity and morphology

One popular way to assess the porosity of the material is to run gas adsorption/desorption experiments with nitrogen as the adsorbate (Fig. 2a and b). After that, we analyzed the obtained data from these measurements using the Brunauer-Emmett-Teller (BET) hypothesis. The type-II isotherms depicted in Fig. 2a illustrate the adsorption/desorption characteristics of nitrogen on the TPP-DBTh and BTPP-DBTh CMPs. These isotherms exhibit considerable increases in nitrogen adsorption at low relative pressures (P/P_0 values below 0.1) and high relative pressures (P/P_0 values above 0.93). The pronounced rise at low pressures implies the existence of micropores, whereas the increase at high pressures signifies the presence of mesopores within the structure of these two CMPs. Fig. 2b and Table S6 indicate that the pore size distribution graph for TPP-DBTh exhibited one broad maximum at 1.29–3.59 nm, whereas BTPP-DBTh displayed two broad peaks at 0.66–1.58 nm and 1.58–3.59 nm. The pore volumes of the CMPs are recorded as 0.44 cm^3 g^{-1} for TPP-DBTh and 0.52 cm^3 g^{-1} for BTPP-DBTh (Table S6). Furthermore, the TPP-DBTh CMP exhibited a surface area of 308 m^2 g^{-1}, while the BTPP-DBTh CMP showed a higher surface area of 388 m^2 g^{-1} (Table S6). This suggests that both TPP-DBTh and BTPP-DBTh CMP possessed substantial surface areas, indicating enhanced porosity and surface reactivity possibilities. The synthesized CMPs' nanoscale morphologies were analyzed employing transmission electron microscopy (TEM) and field emission scanning electron microscopy (FE-SEM). The TEM images of TPP-DBTh CMP revealed the self-assembly of hollow rod-like structures measuring several micrometers in length and averaging 150 ± 70 nm in width (Fig. 2c–e). In contrast, BTPP-DBTh CMP formed irregular, tiny fibers that were curled and had a length of around 600 ± 80 nm and a breadth of around 200 ± 70 nm (Fig. 2f–h). Consequently, the planarity of the TPP-3Br monomer had a significant impact on the crystallite structure of the obtaining CMP; the planar TPP-3Br monomer yielded the rod-like TPP-DBTh CMP [11,38,45,46]. Additionally, the FE-SEM imaging confirmed the rod-like morphology architecture of the TPP-DBTh CMP and the non-spherical BTPP-DBTh CMP (Figs. S14a–d). Furthermore, as demonstrated by our respective elemental mappings produced from energy-dispersive X-ray spectroscopy (EDS) (Figures S14e–h and i–l), it was discovered that both CMPs had a uniform distribution of sulfur, oxygen, nitrogen, and carbon atoms throughout their skeletons.

3.3. Electrochemical properties

With the redox-active structures, high surface areas, excellent thermal stability, and hierarchical micro and mesopore topologies, our TPP-DBTh and BTPP-DBTh CMPs may prove to be useful materials for supercapacitors. As such, we first evaluated the electrochemical capabilities of TPP-DBTh and BTPP-DBTh CMP-coated electrodes by building three-electrode capacitors in an aqueous solution electrolyte containing potassium hydroxide (3M). These supercapacitors used glassy carbon, platinum wire, and Hg/HgO for working, counter, and reference electrodes. The quasi-reversible redox forms were evident in the cyclic

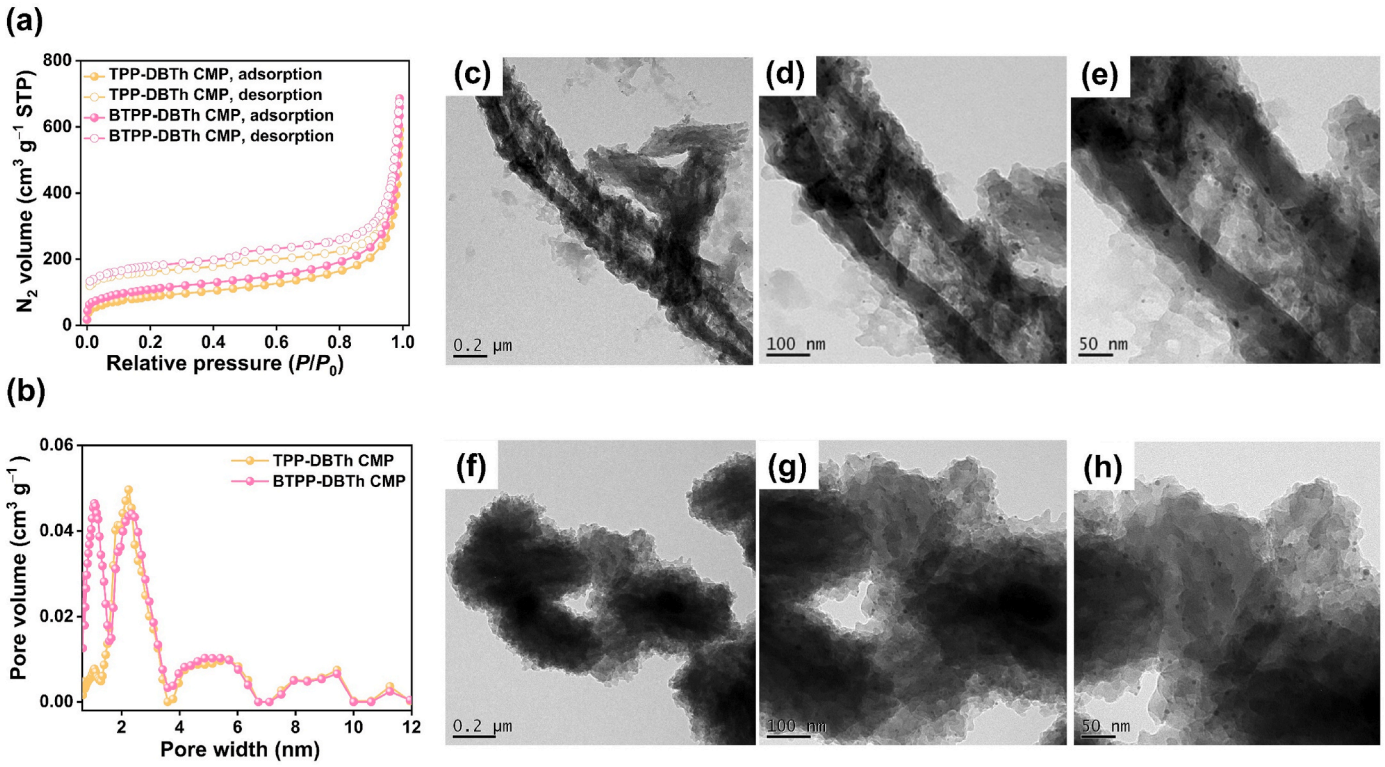

Fig. 2. (a) N_2 adsorption/desorption isotherms and (b) Pore size distribution curves of CMPs. (c–h) HR-TEM images of (c–e) TPP-DBTh CMP and (f–h) BTPP-DBTh CMP.

voltammetry (CV) curves (Fig. 3a and b), showing the pseudocapacitive characteristics of the two types of TPP-DBTh and BTPP-DBTh CMPs in the +0.0 V to −0.7 V potential range at different scan rates that varied from 5 to 200 mV s^{-1} [47]. The TPP-DBTh CMP oxidation and reduction peak potentials were found to be −0.40 and −0.43 V, respectively, within a rate of 5 mVs^{-1}; for BTPP-DBTh CMP, these values were determined to be −0.37 and −0.43 V, respectively (Fig. 3a and b). There was also a positive pattern in the oxidation peak potential rose from 5 to 200 mV s^{-1}, but a negative pattern in the reduction peak potential. As the scanning rate increased, the TPP-DBTh and BTPP-DBTh CMP-coated electrodes' input impedance led to the peak potential gap growing (Fig. 3a and b) [9]. Upon raising the sweep rate, the TPP-DBTh and BTPP-DBTh CMPs' CV curves held their shape, indicating their quick kinetics and high rate capabilities [48]. The tight spacing between the peaks of reduction and oxidation showed a rapid electron transfer between TPP and DBTh and between BTPP and DBTh. All the earlier results confirmed the redox mechanism's quasi-reversibility. Galvanostatic charging and discharging (GCD) experiments were conducted on the TPP-DBTh and BTPP-DBTh CMP-coated electrodes across the identical voltage range, with current densities exceeding 0.5 A g^{-1} to 20 A g^{-1}, to get accurate and specific capacitances. The GCD curves of the two TPP-DBTh and BTPP-DBTh CMPs, depicted in Fig. 3c,d and S15, exhibited an inverted V-shape with pronounced bends, hence affirming the pseudocapacitive properties of the CMPs. The capacitances of the TPP-DBTh and BTPP-DBTh CMPs were calculated using equation S(1) and the discharge period; these were found to be 221.86 and 143.27 F g^{-1} at 0.5 A g^{-1} and 98.07 and 75.30 F g^{-1} at 5 A g^{-1}, respectively (Fig. 3e). In overview, our research revealed that adding redox-active DBTh to the CMP's core significantly affects both its charge energy storage and redox response. TPP-DBTh and BTPP-DBTh CMPs have specific capacitances that are higher than those of similar redox-active materials, such as silsesquioxane-meta-phenylenediamine-based carbon (c-DDSQ-MPD-BMI, 22.86 F g^{-1} at 0.5 A g^{-1}) [49], triphenylpyridine-quinoxalinophenazine (TPP-QP CMP) (24.9 F g^{-1} at 0.5 A g^{-1}) [38], troger-base microporous polymer-based carbons (c-NPIM-EA-TB-70, 41 F g^{-1} at 1.0 A g^{-1}) [50], (c-NPIM-EA-TB-80, 46 F g^{-1} at 1.0 A g^{-1}) [50], H_2 phthalocyanine (HPc CMP/CNTs-2) (53.6 F g^{-1} at 1.0 A g^{-1}) [51], carbazole-thienopyrazine (Cz-TP CMP) (67.38 F g^{-1} at 1.0 A g^{-1}) [8], silsesquioxane-methylene diphenyldiamine-based carbon (c-DDSQMDA-BMI, 73.66 F g^{-1} at 0.5 A g^{-1}) [49], triphenylamine-tetrabenzophenazine (TPA-TBP CMP) (88 F g^{-1} at 1.0 A g^{-1}) [52], CMP films from triphenylamine (TPA) (180 KHz) (91.4 F g^{-1} at 10 mV s^{-1}) [53], Fe phthalocyanine-3 (FeNCCs-3) based CMP/carbon nanotubes (99 F g^{-1} at 1.0 A g^{-1}) [54], Fe phthalocyanine (FePc CMP/CNTs-2) based CMP/carbon nanotubes (100.7 F g^{-1} at 1.0 A g^{-1}) [51], triphenyltriazine-quinoxalinophenazine (TPT-QP CMP) (121.9 F g^{-1} at 0.5 A g^{-1}) [38], anthraquinone-base COF (Dq2Da1-TP, 122 F g^{-1} at 1.56 mA cm^{-2}) [55], triazatruxene-based CMPs (TAT-CMP-1, 141 F g^{-1} at 1.0 A g^{-1}) [56], Pyridine-linked COF (TaPa-Py, 209 F g^{-1} at 0.5 A g^{-1}) [57], and microporous onion-like based carbons (OLC, 211 F g^{-1} at 5 mV s^{-1}) [58] (Fig. 3f and Table S7). Compared to inorganic Faradaic materials, our TPP-DBTh and BTPP-DBTh CMPs offer more advantages because they are easier to synthesize, more affordable to produce, lightweight, environmentally friendly, and moldable. Moreover, because conjugated polymers have mechanical characteristics similar to those of plastic, it has been suggested that they can be stretched, bent, or even flexed [59]. As a result, luminescent diodes or polymeric solar cells can be immediately combined with our CMPs to create low-cost, fully flexible devices in a shorter manufacturing process.

TPP-DBTh CMP redox-dependent process is shown in Figs. S16a and S16b. The DBTh redox interaction pathway involves a two-electron reduction to produce the $DBTh^{2-}$ anion (Fig. S16a) [60]. Fig. S16b demonstrates how the DBTh buildings underwent reduction throughout the process of discharge versus the oxidation process of $DBTh^{2-}$

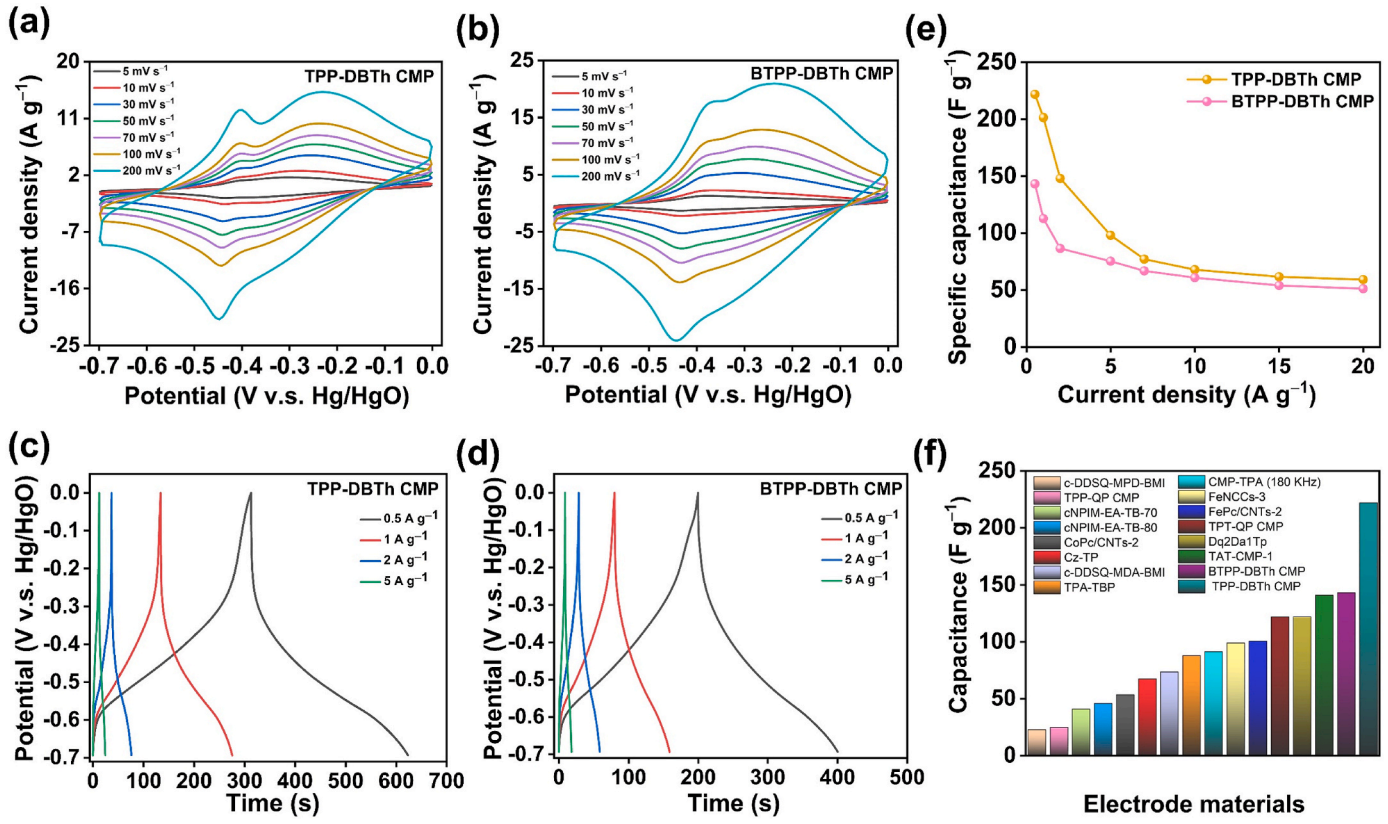

Fig. 3. (a,b) CV profiles and (c,d) GCD profiles of (a,c) the TPP-DBTh and (b,d) BTPP-DBTh CMPs, measured at various scans. (e) Specific capacitances of CMPs at various current densities. (f) Comparison to previously published redox-active CMPs.

occurred during the charge phase. The CV curve's redox peaks at −0.40 and −0.43 V show that DBTh and TPP are stacked up as a single pair (Fig. 3a). BTPP-DBTh CMP redox-dependent process is shown in Figs. S17a and S17b. Two electrons were reduced to produce the $DBTh^{2-}$ anion as part of the redox interaction pathway of DBTh (Fig. S17a) [60]. Fig. S17b demonstrates that while the DBTh buildings underwent reduction during the discharge operation, the $DBTh^{2-}$ experienced oxidation during the charge stages. Overall redox peaks of the CV curve (Fig. 3b) indicate a single pair of combination events between BTPP and DBTh (−0.37 and −0.43 V). The suggested redox mechanisms of the TPP-DBTh and BTPP-DBTh CMPs were validated by conducting cyclic voltammetry of the monomers under identical conditions utilizing a three-electrode setup in an aqueous potassium hydroxide (3M) electrolyte (Figs. S18a–c). The TPP-3Br and BTPP-4Br monomers exhibited rectangular cyclic voltammetry curves. However, the DBTh-2Br had a quasi-reversible redox behavior, indicating that the DBTh unit is the primary component responsible for redox activity in the TPP-DBTh and BTPP-DBTh molecular polymers. Furthermore, the proposed redox process of TPP-DBTh polymer was confirmed by analyzing the chemical alterations of TPP-DBTh polymer during the discharge (reduction) and charge (oxidation) processes by ex-situ FTIR (Fig. S19a–c). A reversible redox reaction occurred in the DBTh structure, as shown by the FTIR spectra, which showed a notable decrease in the carbonyl C=O (1644 cm^{-1}) signal after discharge (Fig. S19b, reduced TPP-DBTh polymer) and a subsequent recovery upon charge (Fig. S19b, oxidized TPP-DBTh polymer). Fig. S19c shows that the C=O functionality is reversible, as demonstrated by the increase and intensity of the C–O (1118 cm^{-1}). To comprehend the kinetic process of charge storage in the constructed electrode, electrochemical impedance spectroscopy (EIS) is typically employed to evaluate the speed at which ions diffuse and the resistivity of charge to flow in the built electrode. The Nyquist charts for the TPP-DBTh and BTPP-DBTh CMP-based electrodes are presented in Fig. 4a. Our electrodes showed tiny semicircles at the high-frequency fields, indicating minimal charge flow impedance and robust connectivity for the electrolyte ions [61]. Our electrodes showed roughly vertical lines at low frequencies, showing their high capacitive properties [60]. By examining the Z′ axis intercept, we were able to determine the intrinsic ohmic resistivity (R_s), which expressed the conductivity of the TPP-DBTh and BTPP-DBTh CMP-based electrodes. An electrode utilizing BTPP-DBTh CMP had superior permeability and reduced charge transfer impedance compared to the TPP-DBTh CMP, as evidenced by the lower R_s value of 9.88 Ω and the bigger R_s value of 26.01 Ω for the BTPP-DBTh CMP (Fig. 4a). The experimental Nyquist charts were fitted using the corresponding circuit as shown in Fig. 4b. The C, R_{ct}, R_s, and W represented the capacitor, resistivity of charge transfer, ohmic resistivity, and Warburg impedance, respectively. Table S8 displays that TPP-DBTh displayed C, R_s, R_{ct1}, R_{ct2} of 6.02 E−5 F, 9.88, 306.1, and 6465 Ω, respectively, whereas BTPP-DBTh displayed C, R_s, R_{ct1}, R_{ct2} of 5.93 E−5 F, 26.01, 780.3, and 11957 Ω, respectively. As a result, The TPP-DBTh CMP-based electrode has higher pseudocapacitance than the BTPP-DBTh electrode due to its lower R_{ct2} value [62]. Bode plots (Fig. 4c) reveal 79 and 107 ms relaxation time constants for TPP-DBTh and BTPP-DBTh CMPs, respectively, confirming their high transport and diffusion characteristics, as supported by Nyquist plots. Furthermore, the electron conductivity of CMPs was assessed at ambient temperature using the four-probe approach. The conductivity of TPP-DBTh CMP is 3.45 Siemen cm^{-1}, surpassing that of BTPP-DBTh CMP (2.70 Siemen cm^{-1}) and exceeding numerous other comparable organic materials (Table S9). The TPP-DBTh CMP electrode has higher conductivity and capacitance. The specific capacitance and lifespan of the associated supercapacitor were significantly increased by adding redox-active DBTh and TPP to the CMP. Furthermore, we subjected our TPP-DBTh and BTPP-DBTh CMP-based electrodes to upwards of 10,000 charging-discharging cycles at an applied current density of 10 A g^{-1}. This allowed us to assess their durability. Given that CMPs were able to retain 77.45 and 87.86 % of their initial specific capacitance, respectively, the TPP-DBTh and BTPP-DBTh CMPs had good cycle stability, as shown in Fig. 4d. After 10,000 charging and discharging cycles, the

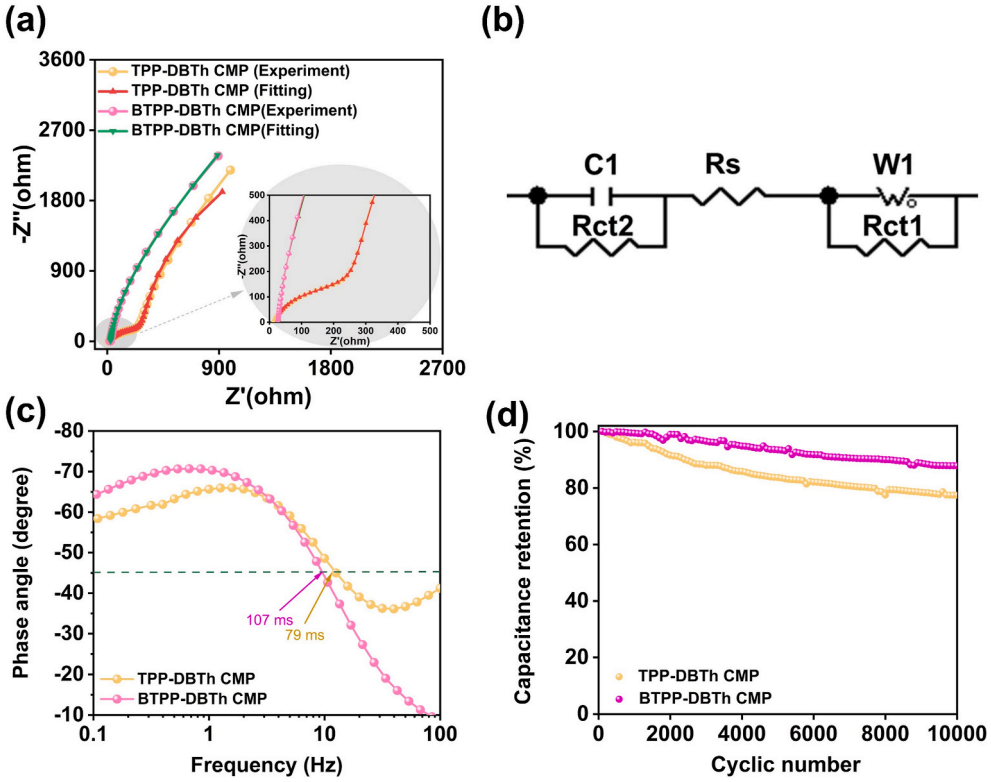

Fig. 4. (a) Nyquist plots and their corresponding fitted plots, (b) equivalent circuits, (c) Bode plots, and (d) cycling stabilities of the TPP-DBTh and BTPP-DBTh CMPs. The stability is measured at a current density of 10 A g^{-1}.

chemical stability of the TPP-DBTh and BTPP-DBTh CMPs was assessed by analyzing their FTIR spectra. The investigation revealed that peaks belonging to conjugated backbones, such as C=C stretching in aromatic rings, stay unchanged, and functional groups related to redox activity, including C=O, C=N, and C−S, exhibit no significant alterations or loss of intensity (Fig. S20). Such data confirmed the high chemical stability of our CMPs.

To understand the capacitive contribution provided by TPP-DBTh and BTPP-DBTh CMPs and the relationship between current (i) and scan rate (v), we employed the power law (Equation (1)) [63].

$$i = av^b \tag{1}$$

The slope of a graph depicting log(i) vs log(v) was employed to ascertain the final value of b. TPP-DBTh CMP has an estimated b value of 0.69 for the cathodic peak and 0.63 for the anodic peak, as illustrated in Fig. 5a. The calculated b value for the BTPP-DBTh CMP was 0.79 for the cathodic peak and 0.72 for the anodic peak, as illustrated in Fig. 5b. The results indicated that the energy storage of these two CMPs may be achieved by the simultaneous operation of diffusion- and capacitance-controlled mechanisms [64,65].

The capacitive contribution to total capacity was determined utilizing a procedure that follows Equation (2) [63].

$$i(V) = k_1 v + k_2 v^{1/2} \tag{2}$$

where $i(V)$ is the total current at a constant potential of V, currents generated by the diffusion-controlled process, and capacitive effects are $k_1 v$ and $k_2 v^{1/2}$. Fig. 5c and d shows that the BTPP-DBTh CMP exhibited a superior capacitive contribution in comparison to the TPP-DBTh CMP, with 10 % and 20 % of the total capacity, respectively, at a scanning rate of 5 mV s^{-1}. As the scanning speed escalated from 5 to 200 mV s^{-1}, capacitance contribution increased to 60 % for TPP-DBTh (Fig. 5e) and 62 % for BTPP-DBTh (Fig. 5f). This occurs because, at elevated scan rates, diffusion of ions into the CMP's network requires less time.

The improved specific capacitance of TPP-DBTh CMP compared to BTPP-DBTh CMP can be attributed to the following advantages: Initially, TPP moiety exhibits greater planarity than the BTPP moiety (Fig. S21), which demonstrates a significant interaction of π-π bonds that facilitates the mobility of electrolytic ions [66,67]. Second, the enhanced electrical conductivity and diminished resistance to charge transmission of the TPP-DBTh CMP, in contrast to the BTPP-DBTh CMP, supported speed rate capabilities. Third, the TPP-DBTh CMP exhibited a hollow rod-like morphology, enhancing electron affinity and increasing ion storage capacity [68].

Therefore, to investigate the prospective application of TPP-DBTh CMP in practically supercapacitor apparatuses, we developed a symmetric supercapacitor (SC) device featuring a two-electrode layout. Two adaptable TPP-DBTh CMP-based electrodes, affixed to carbon sheets, were interposed with a piece of filter paper, utilizing a 3 M potassium hydroxide solution as the electrolyte (Fig. 6a). Under scan speeds between 5 and 500 mV s^{-1} within a potential range of +0.0 to +1.2 volt, the quasi-reversible styles in the CV records showed rapid electrolyte diffusion into the electrode layer (Fig. 6b). These profiles stayed significantly unchanged during the entire sweep [34]. The GCD plots of the TPP-DBTh CMP-based SC system at different current densities ranging from 0.5 A g^{-1} to 10.0 A g^{-1} are displayed in Fig. 6c. Our device's specific capacitance was calculated using equation S(4) and the associated GCD curves. The specific capacitances were 384.61, 311.53, 289.31, 269.23, 251.34, 240.47, 236.45, and 231.45 F g^{-1} at current densities of 0.5, 1, 2, 3, 5, 7, 8, and 10 A g^{-1} (Fig. 6d), respectively, indicating the good performance of our TPP-DBTh CMP-based SC device. These values of capacitance are better than those of symmetric SC devices and SC devices which have already been described before, both of which use similar redox-active materials (94–364 F g^{-1}) (Table S10) [69–74]. The reason for the increased capacitance in the two-electrode device compared to the three-electrode configuration is as follows: In a

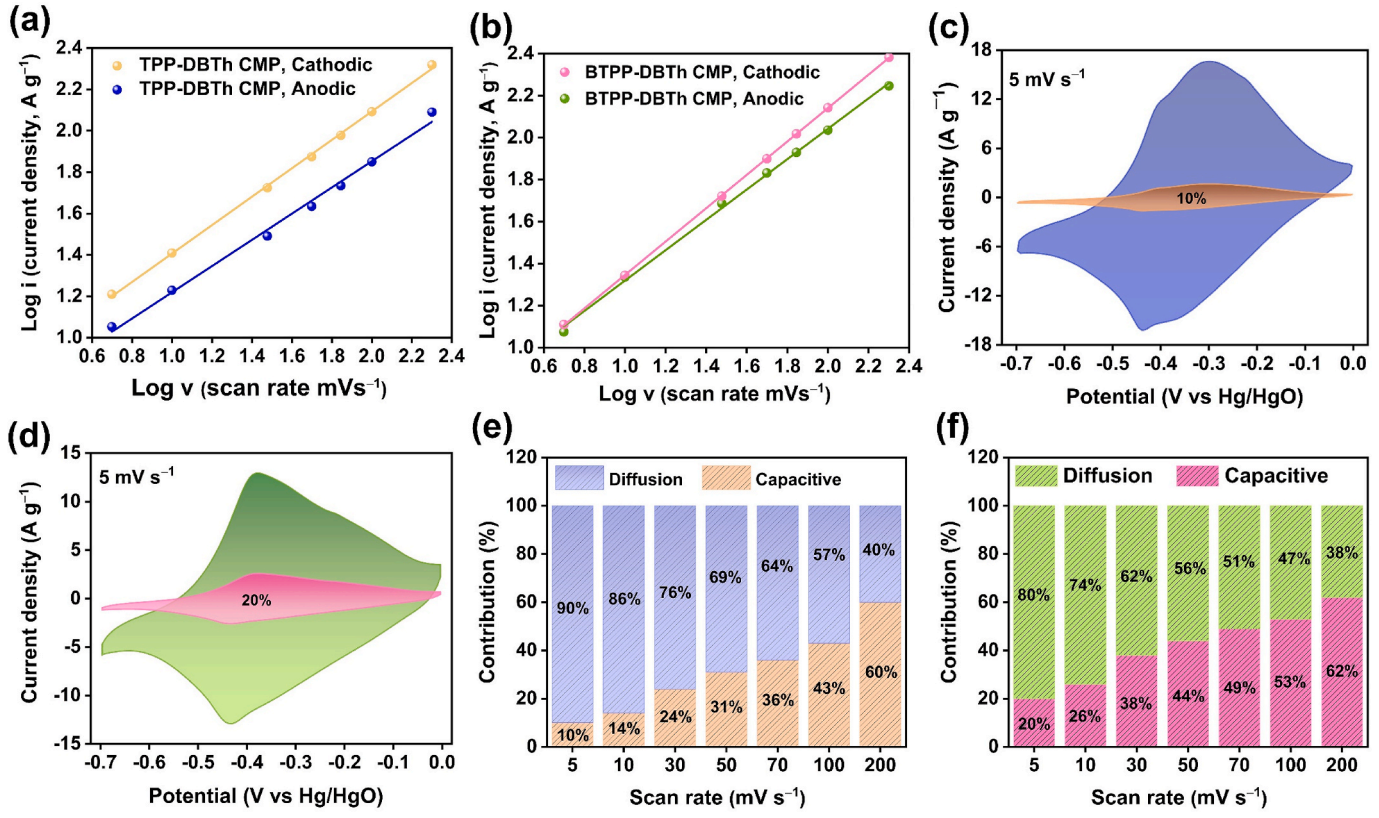

Fig. 5. (a,b) log(i) versus log(v) plots and (c, d) capacitive and diffusion contributions measured at 5 mV s^{-1} of (a,c) TPP-DBTh and (b,d) BTPP-DBTh CMPs. (e,f) Capacitive and diffusion-controlled storage for charges of (e) TPP-DBTh and (f) BTPP-DBTh CMPs at various scans.

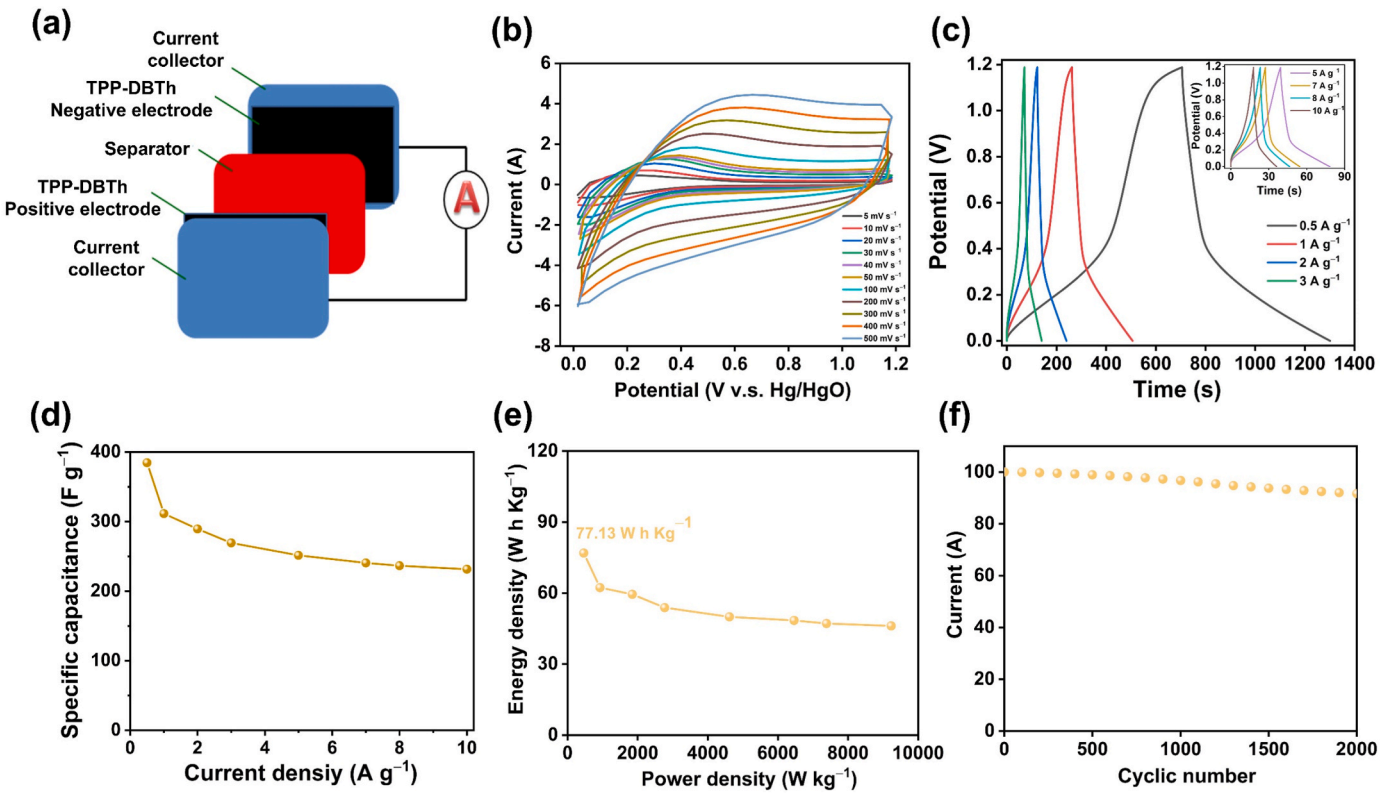

Fig. 6. (a) Schematic design of the TPP-DBTh CMP-based SC device. (b) CV profiles, (c) GCD profiles, (d) Specific capacitances, (e) Ragone plots, and (f) cycling performance measured at a current density of 0.5 A g^{-1} of the TPP-DBTh CMP-based SC device.

three-electrode setup, the working electrode, where capacitance is assessed, is often a solitary electrode, and the voltage is regulated in relation to a reference electrode. The effective surface area in contact with the electrolyte is diminished. In a two-electrode design, both electrodes participate in charge storage, so essentially doubling the active surface area and enhancing capacitance. Furthermore, in the three-electrode setup, only one electrode participates in charge storage, whereas the reference electrode does not store charge. In a device, both electrodes engage in charge storage, resulting in increased electric double-layer capacitance and potential pseudocapacitance contributions from redox-active sites inside the CMP material. Therefore, the elevated capacitance in the TPP-DBTh CMP device, in contrast to the three-electrode configuration, can be attributed to the augmented active surface area, improved ionic transport, and complete use of both electrodes. The Ragone plot (Fig. 6e) indicates that our TPP-DBTh CMP-based symmetric supercapacitor device achieved an optimal energy density of 77.13 W h kg^{-1}, and a power density of 461.53 W kg^{-1}. Based on similar redox-active materials, these values surpass that of earlier published SC and asymmetric SC systems [49–58,75–77], Fig. 6f shows the TPP-DBTh CMP-based SC device's 91.81 % capacitance retention after 2000 charging-discharging cycles at an applied current density of 0.5 A g^{-1}, exhibiting great cycle lifetime and rate proficiency. FTIR spectra were used to evaluate the chemical stability of TPP-DBTh CMP after 2000 charging and discharging cycles. Investigation shows that conjugated backbone peaks, such as C=C stretching in aromatic rings, remain intact; functional groups associated with redox activity, including C=O, C=N, and C−S, do not change or lose intensity (Fig. S22). This result supported our CMP's chemical stability.

4. Conclusions

During this study, we successfully prepared two types of CMPs (TPP-DBTh and BTPP-DBTh CMPs) through coupling polymerization using cheap TPP, BTPP, and DBTh monomers. A novel class of nitrogen-rich pyridine moiety-based electrochemically active polymers has been designed, fabricated, and evaluated as efficient, high-performance supercapacitor electrodes. The chemical structures were confirmed by spectroscopic approaches include FTIR as well as solid-state ^{13}C NMR. Based on the results of the BET and TGA analyses, TPP-DBTh and BTPP-DBTh CMPs demonstrated high specific surface area of up to 308 m^2 g^{-1} and robust thermal stability (701.78 °C Td_{10}, 83.61 % char yield). In particular, the TPP-DBTh CMP showed high electron conductivity 3.45 Siemen cm^{-1} and better three-electrode capacitance of as good as 221.86 F g^{-1} ^{at} a current density of 0.5 Ag^{-1} and good stability (77.45 %) after 10,000 cycles due to its planarity. Furthermore, during 2000 cycles in the two-electrode symmetric supercapacitor apparatus at a broad range of 1.2 V, the TPP-DBTh CMP-based supercapacitor device attained a capacitance of 384.61 F g^{-1}, a capacity retention of 91.81 %, and a highly effective energy density of 77.13 W h kg^{-1} at 461.53 W kg^{-1}. Our research suggests that CMPs' strong specific capacitances, simple synthesis, and high surface areas make them promise for energy storage and conversion technologies.

CRediT authorship contribution statement

Shimaa Abdelnaser: Writing – original draft, Methodology, Investigation, Formal analysis, Data curation, Conceptualization. **Shiao-Wei Kuo:** Resources, Investigation, Funding acquisition, Conceptualization. **Ahmed F.M. EL-Mahdy:** Writing – review & editing, Writing – original draft, Software, Project administration, Formal analysis, Data curation.

Declaration of competing interest

The authors declare that they have no known competing financial interests or personal relationships that could have appeared to influence the work reported in this paper.

Acknowledgements

This study was supported financially by the Ministry of Science and Technology, Taiwan, under contracts 112-2221-E-110-005-MY3 and 113-2218-E-110 -004-.

Appendix A. Supplementary data

Supplementary data to this article can be found online at https://doi.org/10.1016/j.jpowsour.2025.236535.

Data availability

Data will be made available on request.

References

[1] J. Min, G. Yan, A.M. Abed, S. Elattar, M.A. Khadimallah, A. Jan, H.E. Ali, The effect of carbon dioxide emissions on the building energy efficiency, Fuel 326 (2022) 124842, https://doi.org/10.1016/j.fuel.2022.124842.
[2] M.D. Ahmed, K.M. Maraz, Revolutionizing energy storage: overcoming challenges and unleashing the potential of next generation lithium-ion battery technology, Mater. Eng. Res. 5 (2023) 265–278, https://doi.org/10.25082/MER.2023.01.003.
[3] P. Ragupathy, S.D. Bhat, N. Kalaiselvi, Electrochemical energy storage and conversion: an overview, WIREs Energy Environ. 12 (2023), https://doi.org/10.1002/wene.464 e 464.
[4] T.A. Gaber, L.R. Ahmed, A.F.M. EL-Mahdy, Efficient faradaic supercapacitor energy storage using redox-active pyrene-and benzodithiophene-4, 8-dione-tethered conjugated microporous polymers, J. Mater. Chem. 11 (2023) 19408–19417, https://doi.org/10.1039/d3ta03198e.
[5] B. Zhang, C. Wu, G. Meng, F. Xue, S. Lu, Optimal sizing of on board hybrid energy storage devices considering the long-term train operation, IEEE Access 10 (2022) 58360–58374, https://doi.org/10.1109/ACCESS.2022.3179108.
[6] K.C.S. Lakshmi, B. Vedhanarayanan, High-performance supercapacitors: a comprehensive review on paradigm shift of conventional energy storage devices, Batteries 9 (2023) 202, https://doi.org/10.3390/batteries9040202.
[7] K.Y. Lin, A.F.M. EL-Mahdy, Covalent triazine frameworks based on triphenylpyridine building block for high-performance supercapacitor and selective CO_2 capture, Mater. Chem. Phys. 281 (2022) 125850, https://doi.org/10.1016/j.matchemphys.2022.125850.
[8] A.F. Saber, S.U. Sharma, J.-T. Lee, A.F.M. EL-Mahdy, S.-W. Kuo, Carbazole-conjugated microporous polymers from Suzuki–Miyaura coupling for supercapacitors, Polymer 254 (2022) 125070, https://doi.org/10.1016/j.polymer.2022.125070.
[9] S.S. Shah, M.A. Aziz, Properties of electrode materials and electrolytes in supercapacitor technology, J. Chem. Environ. 3 (2024) 1–45, https://doi.org/10.56946/jce.v3i1.309.
[10] T.L. Yang, J.Y. Chen, S.W. Kuo, C.T. Lo, A.F.M. EL-Mahdy, Hydroxyl-functionalized covalent organic frameworks as high-performance supercapacitors, Polymers 14 (2022) 3428, https://doi.org/10.3390/polym14163428.
[11] J. Zhan, A.F.M. EL-Mahdy, Redox-active benzodithiophene-4,8-dione-based conjugated microporous polymers for high-performance faradaic supercapacitor energy storage, Chem. Eng. J. 473 (2023) 145124, https://doi.org/10.1016/j.cej.2023.145124.
[12] D. Cui, Preparation of transition metal oxide mixed graphene electrode materials and its application in supercapacitors, Sci. Technol. Eng. Chem. Environ. Prot. 1 (2024) 1–8, https://doi.org/10.61173/rpqbr688.
[13] B. Moossa, J.J. Abraham, R. Kahraman, S. Al-Qaradawi, T.M. Al Tahtamouni, R. A. Shakoor, Utilization of symmetric electrode materials in energy storage application: a review, Int. J. Energy Res. 46 (2022) 8590–8624, https://doi.org/10.1002/er.7771.
[14] Y. Li, Porous carbonaceous materials for supercapacitors, Porous Carbon Mater. Clean Energy (2024) 252–270, https://doi.org/10.1201/9781003387831-11.
[15] Z. Zhai, L. Zhang a, b, T. Du, B. Ren, Y. Xu, S. Wang, J. Miao, Z. Liu, A review of carbon materials for supercapacitors, Mater. Des. 221 (2022) 111017, https://doi.org/10.1016/j.matdes.2022.111017.
[16] X. Liu, C.-F. Liu, S. Xu, T. Cheng, S. Wang, W.-Y. Lai, W. Huang, Porous organic polymers for high-performance supercapacitors, Chem. Soc. Rev. 51 (2022) 3181–3225, https://doi.org/10.1039/d2cs00065b.
[17] J.H. Wang, A.E. Hassan, A.M. Elewa, Ahmed F.M. EL-Mahdy, Donor–acceptor hetero[6]radialene-based three-dimensional covalent organic frameworks for organic pollutant adsorption, photocatalytic degradation, and hydrogen production activity, J. Mater. Chem. A 12 (2024) 14005–14021, https://doi.org/10.1039/D3TA07691A.
[18] L.R. Ahmed, A.F.M. EL-Mahdy, C.-T. Pan, S.-W. Kuo, A water-soluble copper immobilized covalent organic framework functioning as an "OFF–ON" fluorescent sensor for amino acids, Mater. Adv 2 (2021) 4617–4629, https://doi.org/10.1039/D1MA00234A.
[19] L.R. Ahmed, J. Lüder, C.H. Chuang, A.F.M. EL-Mahdy, Covalent-organic-framework-modified quartz crystal microbalance sensor for selective detection of hazardous formic acid, ACS Appl. Mater. Interfaces 16 (2024) 30408–30420, https://doi.org/10.1021/acsami.4c04630.
[20] S. Luo, E. Almatrafi, L. Tang, B. Song, C. Zhou, Y. Zeng, G. Zeng, Z. Liu, Processable conjugated microporous polymer gels and monoliths: fundamentals and versatile applications, ACS Appl. Mater. Interfaces 14 (2022) 39701–39726, https://doi.org/10.1021/acsami.2c10088.
[21] D. Zhou, K. Zhang, S. Zou, X. Li, H. Ma, Conjugated microporous polymers: their synthesis and potential applications in flexible electrodes, J. Mater. Chem. A 12 (2024) 17021–17053, https://doi.org/10.1039/D4TA02085E.
[22] W. He, J. Duan, H. Liu, C. Qian, M. Zhu, W. Zhang, Y. Liao, Conjugated microporous polymers for advanced chemical sensing applications, Prog. Polym. Sci. 148 (2024) 101770, https://doi.org/10.1016/j.progpolymsci.2023.101770.
[23] H. Sun, W. Chan, H. Zhang, R. Jiao, F. Wang, Z. Zhu, A. Li, Robust synthesis of free-standing films comprising conjugated microporous polymers nanotubes for water disinfection, J. Colloid Interface Sci. 655 (2024) 771–778, https://doi.org/10.1016/j.jcis.2023.11.056.
[24] S.K. Rajput, V.S. Mothika, Powders to thin films: advances in conjugated microporous polymer chemical sensors, Macromol. Rapid Commun. 45 (2024) 2300730, https://doi.org/10.1002/marc.202300730.
[25] N. Naz, M.H. Manzoor, S.M.G. Naqvi, U. Ehsan, M. Aslam, F. Verpoort, Porous organic polymers; an emerging material applied in energy, environmental and biomedical applications, Appl. Mater. Today 38 (2024) 102198, https://doi.org/10.1016/j.apmt.2024.102198.
[26] S. Wang, H. Li, H. Huang, X. Cao, X. Chen, D. Cao, Porous organic polymers as a platform for sensing applications, Chem. Soc. Rev. 51 (2022) 2031–2080, https://doi.org/10.1039/d2cs00059h.
[27] J.H. Wang, C.C. Chang, Z.W. Zhang, A.F.M. EL-Mahdy, Facile metal-free synthesis of pyrrolo[3,2-b]pyrrolyl-based conjugated microporous polymers for highperformance photocatalytic degradation of organic pollutants, Polym. Chem. 13 (2022) 5300–5308, https://doi.org/10.1039/D2PY00658H.
[28] A.F. Saber, A.M. Elewa, H.H. Chou, A.F.M. EL-Mahdy, Donor to acceptor charge transfer in carbazole-based conjugated microporous polymers for enhanced visiblelight-driven photocatalytic water splitting, ChemCatChem 15 (2023) e202201287, https://doi.org/10.1002/cctc.202201287.
[29] A.F. Saber, A.F.M. EL-Mahdy, (E)-1, 2-Diphenylethene-based conjugated nanoporous polymers for a superior adsorptive removal of dyes from water, New J. Chem. 45 (2021) 21834–21843, https://doi.org/10.1039/D1NJ04287D.
[30] S. Muhammad, Z. Wang, J. Li, B. Guo, K. Wang, Design of advanced composite battery materials based on nanoporous functional materials with different dimensionality, Nano Energy 130 (2024) 110161, https://doi.org/10.1016/j.nanoen.2024.110161.
[31] M. Xu, D. Li, Y. Feng, Y. Yuan, Y. Wu, H. Zhao, R.V. Kumar, G. Feng, K. Xi, Microporous materials in polymer electrolytes: the merit of order, Adv. Mater. 36 (2024) 2405079, https://doi.org/10.1016/j.nanoen.2024.110161.
[32] H. Chen, F.-Y. Chu, H.-Y. Zhuang, L. Wang, Z.-M. Ye, W. Dong, Z.-P. Xie, A.-M. Xie, Hyper-crosslinked conjugated microporous polymers with increased micropores promotes confining polymerization for electromagnetic absorption application, Chin. J. Polym. Sci. 41 (2023) 1305–1316, https://doi.org/10.1007/s10118-023-2962-y.
[33] W. Zhang, H. Zuo, Z. Cheng, Y. Shi, Z. Guo, N. Meng, A. Thomas, Y. Liao, Macroscale conjugated microporous polymers: controlling versatile functionalities over several dimensions, Adv. Mater. 34 (2022) 2104952, https://doi.org/10.1002/adma.202104952.
[34] W. Ji, T.-X. Wang, X. Ding, S. Lei, B.-H. Han, Porphyrin-and phthalocyanine-based porous organic polymers: from synthesis to application, Coord. Chem. Rev. 439 (2021) 213875, https://doi.org/10.1016/j.ccr.2021.213875.
[35] Y. Liu, Y. Zhang, Z.-D. Yang, L. Jing, Recent advances in phenazine-linked porous catalysts toward photo/electrocatalytic applications and mechanism, Green Energy Environ. 9 (2024) 1518–1549, https://doi.org/10.1016/j.gee.2023.12.006.
[36] W. Wang, H. Xu, W. Zhao, J. Zhao, M. Jiang, S. Liu, W. Huang, Q. Zhao, Porphyrin-assisted synthesis of hierarchical flower-like polypyrrole arrays based flexible electrode with high areal capacitance, Chem. Eng. J. 428 (2022) 131089, https://doi.org/10.1016/j.cej.2021.131089.
[37] A. Molina, N. Patil, E. Ventosa, M. Liras, J. Palma, R. Marcilla, New anthraquinone-based conjugated microporous polymer cathode with ultrahigh specific surface area for high-performance lithium-ion batteries, Adv. Funct. Mater. 30 (2020) 1908074, https://doi.org/10.1002/adfm.201908074.
[38] M.G. Kotp, S.-W. Kuo, A.F.M. EL-Mahdy, Phenazine-based conjugated microporous polymers: influence of planarity and imine content on energy storage performance, Colloids Surf. A Physicochem. Eng. Asp. 685 (2024) 133210, https://doi.org/10.1016/j.colsurfa.2024.133210.
[39] L. Xu, Y. Zhang, W. Zhou, F. Jiang, H. Zhang, Q. Jiang, Y. Jia, R. Wang, A. Liang, J. Xu, X. Duan, Fused heterocyclic molecule-functionalized N-doped reduced graphene oxide by non-covalent bonds for high-performance supercapacitors, ACS Appl. Mater. Interfaces 12 (2020) 45202–45213, https://doi.org/10.1021/acsami.0c13377.
[40] V. Dhayalan, D. Sharma, R. Chatterjee, R. Dandela, Functionalization of pyridine and quinoline scaffolds by using organometallic Li-, Mg- and Zn-reagents, Eur. J. Org Chem. 26 (2023) e202300285, https://doi.org/10.1002/ejoc.202300285.
[41] A.F.M. EL-Mahdy, C.-H. Kuo, A. Alshehri, C. Young, Y. Yamauchi, J. Kim, S.-W. Kuo, Strategic design of triphenylamine-and triphenyltriazine-based two-dimensional covalent organic frameworks for CO2 uptake and energy storage, J. Mater. Chem. A 6 (2018) 19532–19541, https://doi.org/10.1016/j.matchemphys.2022.125850.
[42] H. Behmadi, S. Naderipour, S.M. Saadati, M. Barghamadi, M. Shaker, N. Tavakoli-Hoseini, Solvent-free synthesis of new 2,4,6-triarylpyridines catalyzed by a

Brønsted acidic ionic liquid as a green and reusable catalyst, J. Heterocycl. Chem. 48 (2011) 1117–1121, https://doi.org/10.1002/jhet.697.
[43] L.R. Ahmed, C.-H. Chuang, J. Lüder, H.-W. Yang, A.F.M. EL-Mahdy, Direct metal-free synthesis of uracil- and pentaazaphenalene-functionalized porous organic polymers via quadruple Mannich cyclization and their nucleobase recognition activities, Macromolecules 55 (2022) 10197–10209, https://doi.org/10.1021/acs.macromol.2c01627.
[44] K.-Y. Chen, A.F.M. EL-Mahdy, Heterosporous phenylpyridine-based covalent organic framework microflowers for highly selective sensing of hydrogen sulfide, ACS Appl. Polym. Mater. 6 (2024) 5452–5461, https://doi.org/10.1021/acsapm.4c00307.
[45] M.G. Kotp, A.F.M. EL-Mahdy, T.-L. Yang, S.-W. Kuo, A pyridinyl-phenanzine conjugated microporous polymer decorated with ultrafine Ag nanoparticles mediates the rapid reduction of nitrophenol, Microporous Mesoporous Mater. 331 (2022) 111669, https://doi.org/10.1016/j.micromeso.2021.111669.
[46] M.G. Kotp, S.U. Sharma, J.-T. Lee, A.F.M. EL-Mahdy, S.-W. Kuo, Triphenylamine-based conjugated microporous polymers as dye adsorbents and supercapacitors, J. Taiwan Inst. Chem. Eng. 134 (2022) 104310, https://doi.org/10.1016/j.jtice.2022.104310.
[47] L. Li, F. Lu, R. Xue, B. Ma, Q. Li, N. Wu, H. Liu, W. Yao, H. Guo, W. Yang, Ultrastable triazine-based covalent organic framework with an interlayer hydrogen bonding for supercapacitor applications, ACS Appl. Mater. Interfaces 11 (2019) 26355–26363, https://doi.org/10.1021/acsami.9b06867.
[48] W. Liu, M. Ulaganathan, I. Abdelwahab, X. Luo, Z. Chen, S.J.R. Tan, X. Wang, Y. Liu, D. Geng, Y. Bao, J. Chen, K.P. Loh, Two-dimensional polymer synthesized via solid-state polymerization for high-performance supercapacitors, ACS Nano 12 (2018) 852–860, https://doi.org/10.1021/acsnano.7b0835.
[49] Z.-Y. Chen, W.-C. Chen, S.-W. Kuo, Enhanced thermal and porous properties of double-decker-shaped polyhedral silsesquioxane-bismaleimide (DDSQ-BMI) nanocomposites for high-performance CO_2 storage and supercapacitors, Polym. Chem. 15 (2024) 553–564, https://doi.org/10.1039/d3py01115a.
[50] J.W. Jeon, J. Shin, J. Lee, J.-H. Baik, R.M.- Evans, N.B. McKeown, T.-H. Kim, J.-C. Lee, S.-K. Kim, B.G. Kim, Hierarchically structured carbon electrodes derived from intrinsically microporous Tröger's base polymers for high-performance supercapacitors, Appl. Surf. Sci. 530 (2020) 147146, https://doi.org/10.1016/j.apsusc.2020.147146.
[51] L. Mei, X. Cui, Q. Duan, Y. Li, X. Lv, H. Wang, Metal phthalocyanine-linked conjugated microporous polymer hybridized with carbon nanotubes as a high-performance flexible electrode for supercapacitors, Int. J. Hydrogen Energy 45 (2020) 22950–22958, https://doi.org/10.1016/j.ijhydene.2020.06.208.
[52] M.G. Kotp, J. Lüder, S.-W. Kuo, A.F.M. EL-Mahdy, Phenazine-integrated conjugated microporous polymers for modulating the mechanics of supercapacitor electrodes, Mater. Adv. 5 (2024) 4142–4150, https://doi.org/10.1039/d3ma00979c.
[53] D.-H. Roh, H. Shin, H.-T. Kim, T.-H. Kwon, Sono-cavitation and nebulization-based synthesis of conjugated microporous polymers for energy storage applications, ACS Appl. Mater. Interfaces 13 (2021) 61598–61609, https://doi.org/10.1021/acsami.1c13755.
[54] L. Mei, X. Cui, J. Wei, Q. Duan, Y. Li, Metal phthalocyanine-based conjugated microporous polymer/carbon nanotube composites as flexible electrodes for supercapacitors, Dyes Pigments 190 (2021) 109299, https://doi.org/10.1016/j.dyepig.2021.109299.
[55] A. Khayum M, V. Vijayakumar, S. Karak, S. Kandambeth, M. Bhadra, K. Suresh, N. Acharambath, S. Kurungot, R. Banerjee, Convergent covalent organic framework thin sheets as flexible supercapacitor electrodes, ACS Appl. Mater. Interfaces 10 (2018) 28139–28146, https://doi.org/10.1021/acsami.8b10486.
[56] X.-C. Li, Y. Zhang, C.-Y. Wang, Y. Wan, W.-Y. Lai, H. Pang, W. Huang, Redox-active triazatruxene-based conjugated microporous polymers for high-performance supercapacitors, Chem. Sci. 8 (2017) 2959–2965, https://doi.org/10.1039/c6sc05532j.
[57] A.M. Khattak, Z.A. Ghazi, B. Liang, N.A. Khan, A. Iqbal, L. Li, Z. Tang, A redox-active 2D covalent organic framework with pyridine moieties capable of faradaic energy storage, J. Mater. Chem. A 4 (2016) 16312–16317, https://doi.org/10.1039/c6ta05784e.
[58] M. Shaibani, S.J.D. Smith, P.C. Banerjee, K. Konstas, A. Zafari, D.E. Lobo, M. Nazari, A.F. Hollenkamp, M.R. Hill, M. Majumder, Framework-mediated synthesis of highly microporous onion-like carbon: energy enhancement in supercapacitors without compromising power, J. Mater. Chem. A 5 (2017) 2519–2529, https://doi.org/10.1039/c6ta07098a.
[59] S.H.K. Paleti, Y. Kim, J. Kimpel, M. Craighero, S. Haraguchi, C. Müller, Impact of doping on the mechanical properties of conjugated polymers, Chem. Soc. Rev. 53 (2024) 1702–1729, https://doi.org/10.1039/d3cs00833a.
[60] V. V Kondratiev, R. Holze, Intrinsically conducting polymers and their combinations with redox-active molecules for rechargeable battery electrodes: an update, Chem. Pap. 75 (2021) 4981–5007, https://doi.org/10.1007/s11696-021-01529-7.
[61] C. Young, J. Kim, Y.V. Kaneti, Y. Yamauchi, One-step synthetic strategy of hybrid materials from bimetallic metal–organic frameworks for supercapacitor applications, ACS Appl. Energy Mater. 1 (2018) 2007–2015, https://doi.org/10.1021/acsaem.8b00103.
[62] K. Li, X. Liu, T. Zheng, D. Jiang, Z. Zhoub, C. Liu, X. Zhang, Y. Zhang, D. Losic, Tuning MnO2 to FeOOH replicas with bio-template 3D morphology as electrodes for high performance asymmetric supercapacitors, Chem. Eng. J. 370 (2019) 136–147, https://doi.org/10.1016/j.cej.2019.03.190.
[63] V.S. Bhat, A. Toghan, G. Hegde, R.S. Varma, Capacitive dominated charge storage in supermicropores of self-activated carbon electrodes for symmetric supercapacitors, J. Energy Storage 52 (2022) 104776, https://doi.org/10.1016/j.est.2022.104776.
[64] Y. Liu, L. Zhou, J. Ouyang, X. Ao, M. Shuang, A.A. Adesina, Electrodeposition nanofabrication of carboxylated carbon nanotubes/α-MnO2 nanorods/polypyrrole composites as high hybrid capacitance electrodes for efficient U (VI) electrosorption, Sep. Purif. Technol. 334 (2024) 125989, https://doi.org/10.1016/j.seppur.2023.125989.
[65] Y. Xu, Y. Du, H. Chen, J. Chen, T. Ding, D. Sun, D.H. Kim, Z. Lin, X. Zhou, Recent advances in rational design for high-performance potassium-ion batteries, Chem. Soc. Rev. 53 (2024) 7202–7298, https://doi.org/10.1039/d3cs00601h.
[66] M. Mahato, S. Nam, R. Tabassian, S. Oh, V.H. Nguyen, I. Oh, Electronically conjugated multifunctional covalent triazine framework for unprecedented CO2 selectivity and high-power flexible supercapacitor, Adv. Funct. Mater. 32 (2022) 2107442, https://doi.org/10.1002/adfm.202107442.
[67] Y. Zhang, B. Zhang, L. Chen, T. Wang, M. Di, F. Jiang, X. Xu, S. Qiao, Rational design of covalent triazine frameworks based on pore size and heteroatomic toward high performance supercapacitors, J. Colloid Interface Sci. 606 (2022) 1534–1542, https://doi.org/10.1016/j.jcis.2021.08.087.
[68] A.F.M. EL-Mahdy, Y.-H. Hung, T.H. Mansoure, H.-H. Yu, T. Chen, S.-W. Kuo, A hollow microtubular triazine- and benzobisoxazole-based covalent organic framework presenting sponge-like shells that functions as a high-performance supercapacitor, Chem. Asian J. 14 (2019) 1429–1435, https://doi.org/10.1002/asia.201900296.
[69] K. Gajewska, A. Moyseowicz, D. Minta, G. Gryglewicz, Effect of electrolyte and carbon material on the electrochemical performance of high-voltage aqueous symmetric supercapacitors, J. Mater. Sci. 58 (2023) 1721–1738, https://doi.org/10.1007/s10853-023-08148-5.
[70] M.R. Biradar, A.M. Kale, B.C. Kim, S. V Bhosale, S. V Bhosale, Perylenediimide/graphite foil-based electrode materials with outstanding cycling stability for symmetric supercapacitor device architectures, Energy Technol. 10 (2022) 2200154, https://doi.org/10.1002/ente.202200154.
[71] A. Narayanan, A. Siddiqa, N.K. Kodihalli, G. Hegde, D.H. Nagaraju, M. Padaki, Designing of a free-standing flexible symmetric electrode material for capacitive deionization and solid-state supercapacitors, ACS Sustain. Chem. Eng. 11 (2023) 3750–3759, https://doi.org/10.1021/acssuschemeng.2c06817.
[72] K. Mani, T. Subramaniam, S. Ramachandran, D. S, Unveiling manganese malate as an electrode material for supercapacitors, Electrochim. Acta 511 (2025) 145395, https://doi.org/10.1016/j.electacta.2024.145395.
[73] Z. Li, J. Li, B. Wu, H. Wei, H. Guo, Z.M. El-Bahy, B. Liu, M. He, S. Melhi, X. Shi, S. D. Mekkey, Y. Sun, B.B. Xu, Z. Guo, Interfacial-engineered robust and high performance flexible electrodes for electrochemical energy storage, J. Mater. Sci. Technol. 203 (2024) 201–210, https://doi.org/10.1016/j.jmst.2024.02.084.
[74] T. Wang, L. Peng, B. Deng, F. Yuan, J. Guo, Q. Liu, D. Wua, Cellulose degradation of cottonseed meal derived porous carbon for supercapacitor, Fuel 357 (2024) 129653, https://doi.org/10.1016/j.fuel.2023.129653.
[75] B. Ambrose, K. Nasrin, M. Arunkumar, A. Kannan, M. Sathish, M. Kathiresan, Viologen-based covalent organic polymers: variation of morphology and evaluation of their ultra-long cycle supercapacitor performance, J. Energy Storage 61 (2023) 106714, https://doi.org/10.1016/j.est.2023.106714.
[76] N. An, M. Wei, C. Guo, J. Xin, C. Meng, D. Sun, Y. Lei, Z. Hu, X. Dong, L. Zhao, Integrated N-doped carbon electrodes with regional synergistic energy storage mechanisms for zinc-ion hybrid supercapacitors, J. Power Sources 599 (2024) 234212, https://doi.org/10.1016/j.jpowsour.2024.234212.
[77] N. Guo, A. Liu, W. Luo, R. Ma, L. Yan, L. Ai, M. Xu, L. Wang, D. Jia, Hybrid nanoarchitectonics of coal-derived carbon with oxidation-induced morphology-selectivity for high-performance supercapacitor, J. Colloid Interface Sci. 639 (2023) 171–179, https://doi.org/10.1016/j.jcis.2023.02.067.